

Band Gap Engineering of Paradigm MOF-5

Li-Ming Yang,*^{†,‡,§} Guo-Yong Fang,[†] Jing Ma,[†] Eric Ganz,^{||} and Sang Soo Han[§]

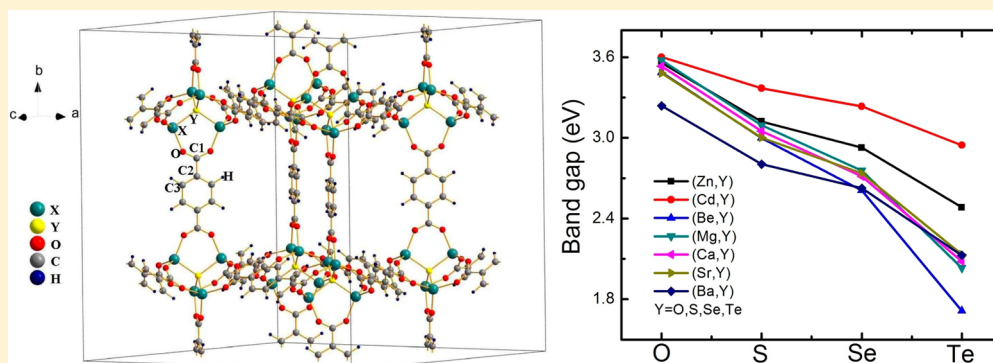
[†]Department of Chemistry, Institute of Theoretical and Computational Chemistry, Key Laboratory of Mesoscopic Chemistry of MOE, Nanjing University, Nanjing, 210093, People's Republic of China

[‡]Center of Theoretical and Computational Chemistry, Department of Chemistry, University of Oslo, P.O. Box 1033 Blindern, N-0315 Oslo, Norway

[§]Center for Computational Science, Korea Institute of Science and Technology, Hwarangno 14-gil 5, Seongbuk-gu, Seoul 136-791, Republic of Korea

^{||}Department of Physics, University of Minnesota, Minneapolis, Minnesota 55455 United States

S Supporting Information



ABSTRACT: Recently, metal–organic frameworks (MOFs) have demonstrated great potential in photocatalysis and luminosity applications. However, most MOFs are dielectrics with substantial band gaps which limits applications of MOFs in the visible-light region. In this paper, we systematically tune the band gap of paradigm MOF-5 by substituting new atoms for the corner elements (X_4Y), in computer simulations using density functional theory. The new proposed materials are labeled X_4Y –MOF-5 ($X = \text{Zn, Cd, Be, Mg, Ca, Sr, Ba}; Y = \text{O, S, Se, Te}$). These new materials have band gaps ranging from 1.7 to 3.6 eV. The underlying mechanism of tunability of band gap can be ascribed to the electronic states of chalcogen atoms (O, S, Se, Te) in the X_4Y nodes and carbon atoms in the BDC linkers. The substantial tunability of band gap leads to a large absorption range covering the visible spectrum. These proposed new materials may be useful for future applications in visible-light promoted photocatalysis or luminosity. The tunability of other properties such as bulk modulus, chemical bonding, and optical properties were also investigated. These novel materials may also be useful for devices in nanoelectronics or optoelectronics.

I. INTRODUCTION

Metal–organic frameworks (MOFs),^{1,2} as a new generation of porous materials, have attracted great attention in the past two decades due to their modular structures, exotic and interesting properties, and wide applications in various aspects such as gas storage, separation, sensor, catalysis, luminescence, and drug delivery.^{1,2} MOFs have had a remarkable impact in the fields of chemistry, physics, materials sciences, and engineering.^{1,2}

Recently, MOFs have demonstrated great potential in photocatalysis,^{3–5} as a “green” technology for the treatment of all kinds of contaminants. This can have many advantages over other treatment methods, such as the use of the environmentally friendly oxidant O_2 , ambient temperature reaction conditions, and oxidation of organic compounds, even at low concentrations. Moreover, MOFs have been tested as good candidates for solar energy harvesting.⁶ However, the large band gap (3.4–4.0 eV)^{4,5,7} of paradigm MOF-5⁸ limits

further application of this material in the visible-light region. Because a large proportion of the solar spectrum and most artificial light sources are in the visible spectrum, it is clear that the development of photocatalysts with high activity under visible-light irradiation is indispensable. Thus, the development of novel MOFs materials with visible light response is highly desirable.

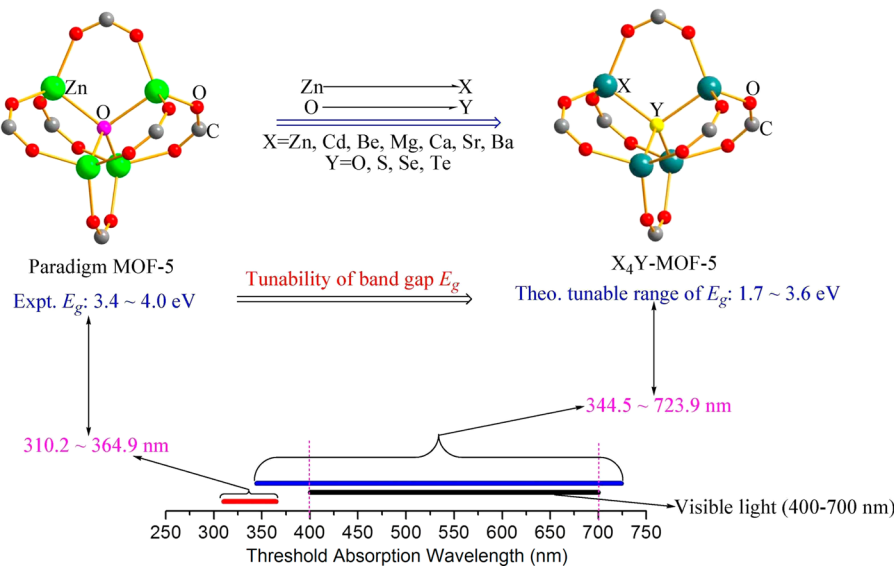
It should be pointed out that the experimental band gap of MOF-5 ranges from 3.4 to 4.0 eV depending on several factors (crystal size, concentration, temperature, preparation method, and sample treatment) during synthesis.^{4,5,7} There has been some controversy regarding the details of the luminescence mechanisms of MOF-5. Early studies suggested quantum dot

Received: February 17, 2014

Revised: April 7, 2014

Published: April 8, 2014

Scheme 1. Substantial Tunability of the Band Gap (E_g) of Paradigm MOF-5 via the Substitution of Zn_4O with X_4Y in the Node and Its Corresponding Absorption Region in the Visible Light Spectra^a



^a X = Zn, Cd, alkaline-earth metals; Y = chalcogen atoms. The red horizontal line corresponds to the threshold absorption wavelength range of experimental band gap for MOF-5. The blue horizontal line is the range for the computational analogues X_4Y -MOF-5. The absorption spectrum covers the whole region of visible light after substitution.

like luminescence behavior of the secondary building units, derived from comparison with the luminescence of bulk and nanosize ZnO .⁷ Further investigations demonstrated that ZnO impurities in the material gave rise to the emission assigned to the quantum dot like luminescence and that pure MOF-5 displays a luminescence behavior that is more closely relevant to that of the ligand.⁹ However, the exact nature of the luminescence of MOF-5 is still under dispute with ligand–ligand charge transfer,¹⁰ ligand-centered,⁹ and ligand–metal charge transfer¹¹ mechanisms as primary suggestions. Heine et al.¹² have reviewed the conflicting interpretations regarding the underlying luminescence mechanism of MOF-5.

In this work, our calculations focus on the intrinsic properties based on the ideal perfect crystal without defects and impurities. This is, to some extent, different from the experimentally synthesized samples, which may contain defects and impurities, which may potentially affect the optical properties.

The band gap of MOF-5 corresponds to UV light absorption. Thus, it is of great interest to systematically manipulate the band gap of MOF-5 analogues for visible light absorption, which will greatly trigger interests in utilizing MOFs as visible light photocatalysts, luminescent materials, or optoelectronic elements. How to effectively tune the band gap and extend the absorption spectrum to visible light range is a big challenge.

Here, we demonstrate systematic substitution engineering of band gap, crystal lattice, bulk modulus, chemical bonding, and optical properties of MOF-5 by joint combination of different metal (X) and anion (Y) atoms [i.e., X_4Y -MOF-5 (X = Zn, Cd, Be, Mg, Ca, Sr, Ba; Y = O, S, Se, Te)] using density functional theory (DFT) calculations. Interestingly, the band gap can be very effectively and substantially tuned from 3.6 to 1.7 eV. In view of the potential applications of MOFs in photochemistry, luminescence, and optoelectronics, the optical response properties of this new X_4Y -MOF-5 series were systematically investigated. The newly proposed scheme could be generally applicable to many other different types of MOFs.

II. COMPUTATIONAL DETAILS

The Vienna ab initio simulation package (VASP)^{13,14} with generalized gradient approximation (GGA)^{15–17} has been used for the total-energy calculations to study the structural stability and to establish equilibrium structural parameters. The projector-augmented-wave (PAW)¹⁸ Perdew, Burke, and Ernzerhof (PBE)¹⁷ pseudopotentials were used to describe the ion–electron interactions. A criterion of 0.01 meV/atom was placed on the self-consistent convergence of the total energy, and all calculations were made with a plane-wave cutoff of 500 eV, which guarantees that absolute energies are converged to within a few meV/formula unit. This has been tested to be accurate and reliable for our X_4Y -MOF-5 systems. Brillouin-zone integration was performed with a Gaussian broadening of 0.2 eV during all relaxations. The atoms were relaxed toward equilibrium until the Hellmann–Feynman forces were less than 10^{-3} eV/Å. For IRMOF materials these calculations can be performed with a single k-point at the Γ -point.^{19,20} We use the Γ -point in all VASP calculations. To understand the chemical bonding and interactions between constituents in X_4Y -MOF-5, charge density, charge transfer, and electron localization function (ELF)^{21–24} analyses were performed using VASP.

We used ultrasoft pseudopotential PBE-GGA implemented in CASTEP for the calculations of optical properties for X_4Y -MOF-5 series at the theory level of fine, with energy cutoff of 340 eV, number of k-points in the SCF calculation and Brillouin zone integration: $1 \times 1 \times 1$, SCF tolerance = 10^{-5} eV/atom, and band energy tolerance = 10^{-5} eV. The number of empty bands for the optical calculations was increased to 999. The method used for the calculation of optical properties has been proven to be reasonable and compared favorably with corresponding experimental spectra in a series of previous papers from our group.^{18,25–32} This gives us confidence to use the same method in the present systems. For the population analysis (including Mulliken effective charge and bond overlap population), we applied on the fly³³ pseudopotential PBE-GGA at the level of fine.^{19,25–32} To gauge the bond strength and character of bonding, we have analyzed bond overlap population (BOP) values estimated on the basis of the Mulliken population as implemented in the CASTEP code.³⁴

III. RESULTS AND DISCUSSION

A. Structural Details. MOF-5 consists of Zn_4O tetrahedral nodes linked by 1,4-benzenedicarboxylate (BDC) forming the

face-centered cubic (FCC) with $Fm\bar{3}m$ symmetry. Structural analogues can be obtained via the substitution of Zn_4O by X_4Y with different metal and anionic atoms in the nodes while keeping the linkers unchanged. This produces the series X_4Y -MOF-5 ($X = Zn, Cd, Be, Mg, Ca, Sr, and Ba; Y = O, S, Se, and Te$). The conventional cell of X_4Y -MOF-5 has 424 atoms with cubic $Fm\bar{3}m$ symmetry and contains eight formula units of $(X_4Y)(BDC)_3$. Its primitive cell has 106 atoms, including two nodes and six linker molecules, corresponding to two $(X_4Y)(BDC)_3$ formula units. The crystal structure of X_4Y -MOF-5 is illustrated in Figure 1. Different crystallographic sites

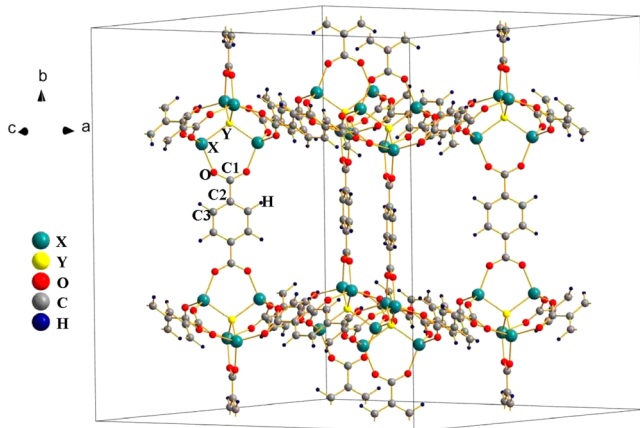


Figure 1. Crystal structure of X_4Y -MOF-5 in the face-centered cubic $Fm\bar{3}m$ symmetry. We distinguish the atoms with labels X (= Zn, Cd, Be, Mg, Ca, Sr, Ba), Y (= O, S, Se, Te), O, C1, C2, C3, and H.

in X_4Y -MOF-5 include one type of X, one type of Y, one type of O, three types of C, and one type of H. For the convenience of our discussion, we classify the whole series into seven subseries (Zn_4Y through Ba_4Y).

B. Crystal Structural Optimization of X_4Y -MOF-5 from Total-Energy Calculation. We built the X_4Y -MOF-5 structures by replacing the metal and anionic atoms of node from Zn and O to X and Y in MOF-5, and meanwhile keeping the space group and skeleton unchanged using Materials Studio 5.0³⁵ to generate the starting geometry of analogues for the structural optimization by VASP calculations. The theoretical

ground-state structure was obtained from this starting geometry by full optimization, i.e., the atomic positions and cell parameters were fully relaxed without any symmetry constraints. The calculated total energy as a function of volume was fitted to three different equations of state (Murnaghan,³⁶ Birch–Murnaghan,³⁷ and Universal EOSs³⁸) to calculate the bulk modulus (B_0) and its pressure derivative (B'_0). The bulk modulus is plotted in Figure 2. Moreover, the present results are comparable to the available experimental data and previous theoretical results for MOF-5 (see Supporting Information (SI) Table S1). The bulk modulus ranges from 8.3 to 19.6 GPa. This may find applications of MOFs as soft materials with different bulk moduli for specific applications. In general, the values of the lattice parameters slightly increase, and the bulk moduli slightly decrease within each subseries when moving from O → Te. From Figure 2 one can see that for (Zn, Y), (Cd, Y), (Be, Y), and (Mg, Y), the lattice parameters slightly increase gradually when moving from O → S → Se → Te. Overall, we observe a range of 24.4 to 29.8 Å for the lattice constant.

C. Evaluation of Formation Energy and Considerations of Synthesis Variability. Data on formation energies constitute an excellent means to establish whether theoretically predicted phases are likely to be stable and also such data might serve as a guide to evaluate possible synthesis routes. For the exploration of the thermodynamic feasibility of synthesizing these predicted compounds from the elements (eq 1) we have computed the total energies for C ($R\bar{3}m$), H_2 ($P4/mmm$), O_2 ($P4/mmm$), S ($Fddd$), Se ($P2_1/c$), Te ($P3_121$), Zn ($P6_3/mmc$), Cd ($P6_3/mmc$), Be ($P6_3/mmc$), Mg ($P6_3/mmc$), Ca ($Fm\bar{3}m$), Sr ($Fm\bar{3}m$), and Ba ($I\bar{m}\bar{3}m$) in their bulk structures. The reaction energies for MOF formation were calculated from the difference in the total energy between the products and reactants (eq 1). The calculated results (SI Table S3) are plotted in Figure 3, and establish that all these compounds are possible to be synthesized in stable forms since eq 1 shows largely exothermic reactions for present X_4Y -MOF-5 series. It should be pointed out that this method has been successfully applied to different experimentally synthesized MOFs and found to be reliable by several papers in our group.^{19,25–32}

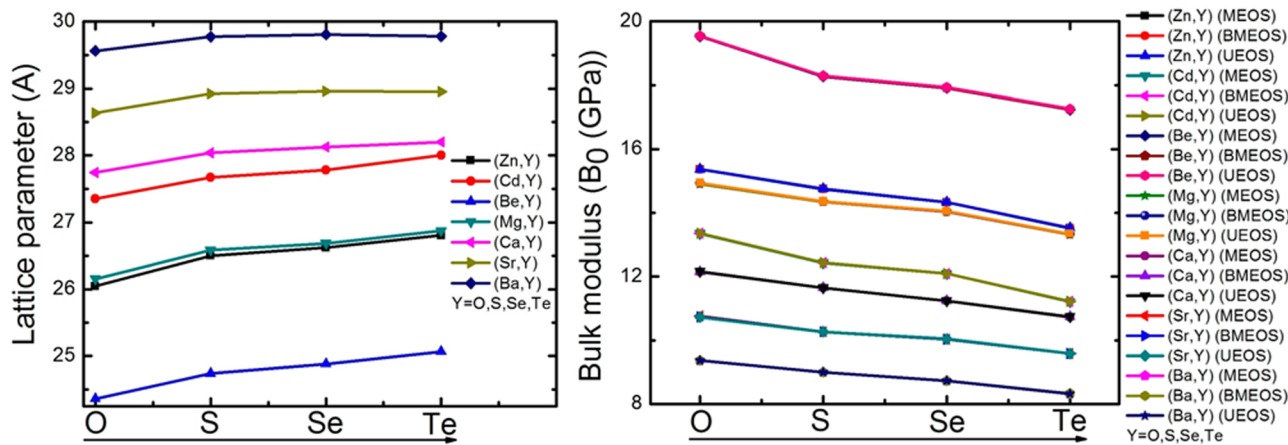
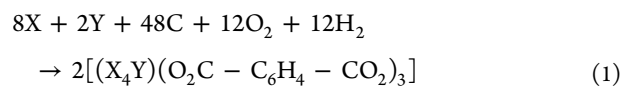


Figure 2. Evolution of lattice parameters (Å) (left) and of bulk modulus (right) from three different equations of state (EOS), i.e., Murnaghan EOS (MEOS), Birch–Murnaghan 3rd-order EOS (BMEOS), and Universal EOS (UEOS) of novel materials (X, Y) (X = Zn, Cd, Be, Mg, Ca, Sr, Ba; Y = O, S, Se, Te) series in the cubic $Fm\bar{3}m$ symmetry (no. 225).

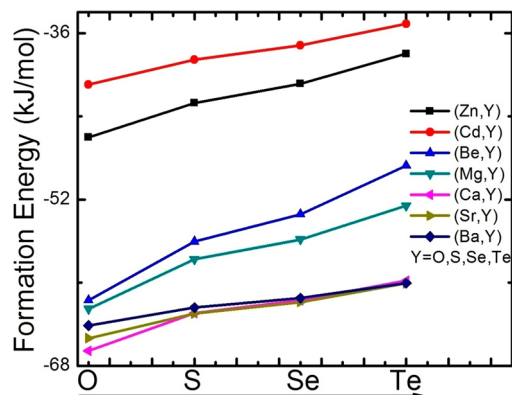


Figure 3. Evolution of the calculated formation energies including partial data from refs 19, 25, and 29.

The large negative magnitude (from -35 to -69 kJ/mol) of the calculated formation enthalpies suggests that all the proposed materials have high stabilities and may be experimentally synthesized under suitable conditions. Most of the new materials have larger formation energy than the existing prototype MOF-5.⁸ We also observe that the formation energies of the alkaline-earth metals subseries are much higher than those of the Zn and Cd subseries, indicative of very high stability of alkaline-earth MOFs. This has been demonstrated by the fact that a series of alkaline-earth MOFs (e.g., Be,^{39,40} Mg,^{41–45} Ca,^{46–48} Sr,^{48,49} Ba,^{50–56} etc.) with interesting properties were experimentally synthesized recently. The magnitude of formation energy of each material is monotonically decreasing within subseries when moving from O \rightarrow S \rightarrow Se \rightarrow Te. More interestingly, one could systematically manipulate the formation energy via different combination of metal and chalcogen atoms in the nodes. Alternatively, one could calculate formation energy based on individual submolecules, for example, see Kuc et al.⁵⁷ One should keep in mind that the kinetics and temperature effects might have large impact on the synthesis of target MOFs materials.^{50,58}

D. Electronic Structures and Band Gap Engineering of X₄Y-MOF-5. The calculated band structures for the whole X₄Y-MOF-5 series can be found in SI Figures S1–S21. From the band structures one can obtain the band gap E_g for all materials, which is plotted in Figure 4. The calculated band gap values (SI Table S4) for the X₄Y-MOF-5 series cover a wide range from 1.71 to 3.60 eV. Therefore, all materials are semiconductors. The corresponding wavelengths λ of absorption

range from 345 to 724 nm in the spectrum. One can see (in Figure 4) that from O \rightarrow S \rightarrow Se \rightarrow Te, the band gap is gradually decreasing, but the corresponding wavelength of absorption is gradually increasing. Thus, the E_g and λ can be systematically tuned. This is in contrast to our previous conclusion that the band gap is almost constant irrespective of the change of the metal atoms, which was observed in a series of IRMOFs, e.g., M-IRMOF-1,^{19,25,29} -10,²⁶ -14,²⁷ -993,²⁸ (M = Zn, Cd, alkaline-earth metals), A-IRMOF-M0,³¹ (A = Zn, Cd, alkaline-earth metals) and M4O(FMA)₃ (M=Zn and Cd)³⁰ in our previous studies.

From SI Figures S1–S21 one can see that the bands in the valence band (VB) as well as in the conduction band (CB) are very flat and with very small dispersion, a common feature for these IRMOFs materials.^{19,25–31,59} This is common for porous materials. As discussed in Section III.A, the X₄Y nodes are well isolated and connected by organic molecular linkers. This well isolated structural arrangement makes molecular like electronic structures and this is the origin for the almost dispersionless bands in X₄Y-MOF-5.

For further analysis of the underlying mechanism of the tunability of the band gap, calculations of partial and total density of states (PDOS and TDOS) were performed. All the PDOS plots can be found in SI Figures S22–S28.

From the PDOS, one can see that the electronic states of the Y (= O, S, Se, Te) atoms in the X₄Y nodes and C atoms in the linkers (BDC) determine E_g. We plot the PDOS for representative subseries (Zn, Y) in Figure 5 from -1.5 to 2.5 eV to highlight the regions responsible for the band gap change. Note that the PDOS of the H atoms does not influence E_g. The p-states of C1, C2, C3, and O atoms gradually shift to lower energy for (Zn, Y), i.e., the p-states of the BDC linkers are shifted to the lower energy as Y changes from O to Te, whereas the p-states of Y atoms gradually shift to higher energy. Therefore, E_g monotonically decreases for (Zn, Y) subseries. It is the same story for other subseries (see SI Figure S29). The total density of states for each subseries is displayed in SI Figure S30. One can see that the general characteristics of TDOS of each material are similar within each subseries, e.g., the general shapes and major peaks are similar for (Zn, O), (Zn, S), (Zn, Se), and (Zn, Te) within (Zn, Y) subseries.

Sometimes DFT calculations will underestimate the band gaps compared with the experimental values (such as for elemental semiconductors). However, in the case of MOF-5, it appears that the DFT results agree well with experiment. Recent calculations by Ji et al.¹⁰ found that the absorption line

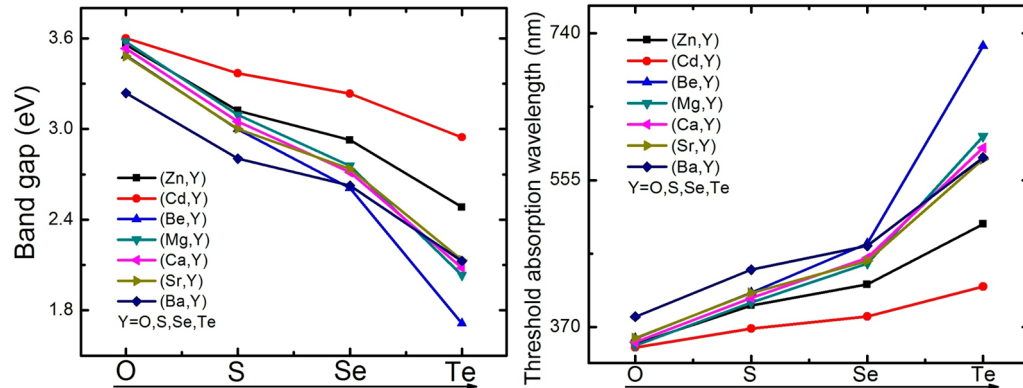


Figure 4. Evolution of the calculated band gap (left) and corresponding threshold absorption wavelength (right) for X₄Y-MOF-5.

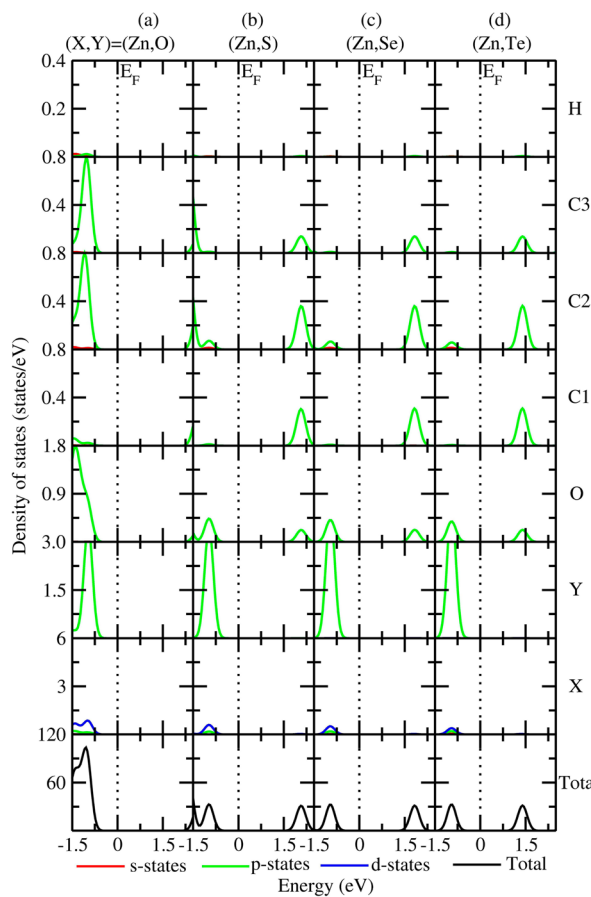


Figure 5. Partial density of states for the subseries (X, Y) ($X = \text{Zn}$; $Y = \text{O}, \text{S}, \text{Se}, \text{Te}$) in the range -1.5 to 2.5 eV. Columns (a–d) represent different materials. Rows represent the PDOS contributions from different atoms. The last row shows total density of states for each material.

for clean MOF-5 is at 349 nm. This agrees very closely with recent experiments made with MOF-5 free of ZnO impurities,⁹ which also produced adsorption at 350 nm corresponding to a 3.5 eV bandgap. This also agrees well with previous DFT computations by Yang et al.²⁵ Because the current materials are derived from MOF-5, and have the same crystal structures and linkers, this gives us confidence that the DFT results may turn out to be relatively accurate. Ultimately, this will need to be tested by comparison with experiment. In the case that the DFT bandgap does not agree with the actual bandgap, this is often fixed by a “scissor” operation.⁶⁰ Alternatively, more accurate band gaps can often be obtained from more computationally intensive hybrid functionals^{61–63} and GW⁶⁴ methods, or other methods which are beyond the scope of this work.

E. Chemical Bonding. A consistent view of the chemical bonding in $X_4Y\text{-MOF-5}$ emerges from the partial density of states (PDOS), charge density/transfer, electron localization function (ELF),^{21–24} Bader topological analysis^{65–67} (bader charge, BC), Mulliken population analysis⁶⁸ (Mulliken effective charge, MEC), bond overlap populations (BOP), and electron configuration (EC). The details of these results are given in the SI (PDOS: Figures S22–S28; charge density/transfer and ELF plots: Figures S31–S51; MEC, BC, BOP, and EC: Figures S52–S53 and Tables S5–S12).

The calculated MEC values (SI Tables S5–S11) are $+0.96$ to $+1.58$ lel for X and -0.14 to -1.28 lel for Y , indicating mainly ionic interactions. The values of MEC of both X and Y are decreasing, whereas that of O (in BDC) is almost constant (-0.6 to -0.7 lel) within each subseries when Y is moving from O to Te . One should keep in mind that MEC is sensitive to the basis set, and only qualitative information about the evolution trend should be expected from MEC analysis. The Mulliken population analysis also provides $X\text{-}Y$ bond overlap populations (BOP values, SI Tables S5–S11) in the range $0.07\text{--}0.55$, which is much smaller than that of normal covalent bond indicating dominantly ionic interactions. In general, the order of covalent component within $X\text{-}Y$ bonds is $\text{Zn}\text{-}Y > \text{Cd}\text{-}Y > \text{Be}\text{-}Y > \text{Mg}\text{-}Y > \text{Ca}\text{-}Y \geq \text{Sr}\text{-}Y > \text{Ba}\text{-}Y$. Within each subseries, the order of covalency of $X\text{-}Y$ generally follows the order of $X\text{-}O < X\text{-}S < X\text{-}Se < X\text{-}Te$. This is in accord with electronegativity trends within the group VIa.

Moreover, from MEC analysis, one can also identify the distribution of electrons in different orbitals of each atoms, i.e., electron configuration (EC) (SI Tables S5–S12) for each material. For transition metals Zn and Cd, the electrons (~ 10 lel) located in d orbitals together with a small part (0.4–0.5 lel) distributed in s and p orbitals. Whereas, for the main group metal Be, the electrons dominantly distributed in s orbitals (~ 2.3 lel), together with a small part located in p orbitals (0.6–0.7 lel); for Mg, the electrons majorly reside in p orbitals (~ 6.2 lel), with minority in s orbitals (0.2–0.3 lel); for Ca, Sr and Ba, the s (~ 2.1 lel) and p (~ 6 lel) orbitals accommodate the main electrons, with only a small part located in d orbitals (0.5–0.6 lel). The summarization of EC and its simplification are listed in SI Table S12 for the whole $X_4Y\text{-MOF-5}$ series. One can get the overall pictures of the distribution of electrons in different orbitals and the hybridization of atoms within different materials.

The Bader Charge analysis (SI Tables S5–S11) for X and Y/O in the series indicates that the interaction between X and Y/O is almost ionic, since nearly two electrons (+1.2 to +2.0 lel) are transferred from X to Y/O .

To summarize the findings, the bonding between X and Y/O (Y = chalcogen atoms, O is from linker BDC) is mainly ionic, but with partial covalent character. The difference in chemical bonding comes from the different ratio between ionicity and covalency between different $X\text{-}Y$ bonds. For example, there is more covalency and less ionicity in $\text{Be}\text{-}Y$ bond comparing to $\text{Ba}\text{-}Y$ bond with the same Y atoms even though both have mainly ionic components. At the extremes, more covalency and less ionicity are seen in the $\text{Be}\text{-}\text{Te}$ bond compared to the $\text{Ba}\text{-}\text{O}$ bond, even though both are mainly ionic. More generally, more covalency and less ionicity is found in $X\text{-}Y$ with the same X , when Y is moving from O to Te . Finally, we can conclude that the main character of chemical bonding between constituents is similar for each material within $X_4Y\text{-MOF-5}$ series.

F. Tuning Optical Response. Systematic tunability of the optical response of materials is useful for applications in optoelectronics, photoconducting materials, and light energy conversion. We demonstrate the engineering of the optical properties of MOFs, which may pave the way for use of these MOFs in optoelectronic devices. The central quantity of interest in optical properties is the dielectric function $\epsilon(\omega)$, which describes the linear response of the system to electromagnetic radiation. The imaginary part $\epsilon_2(\omega)$ can be derived from interband optical transitions between the

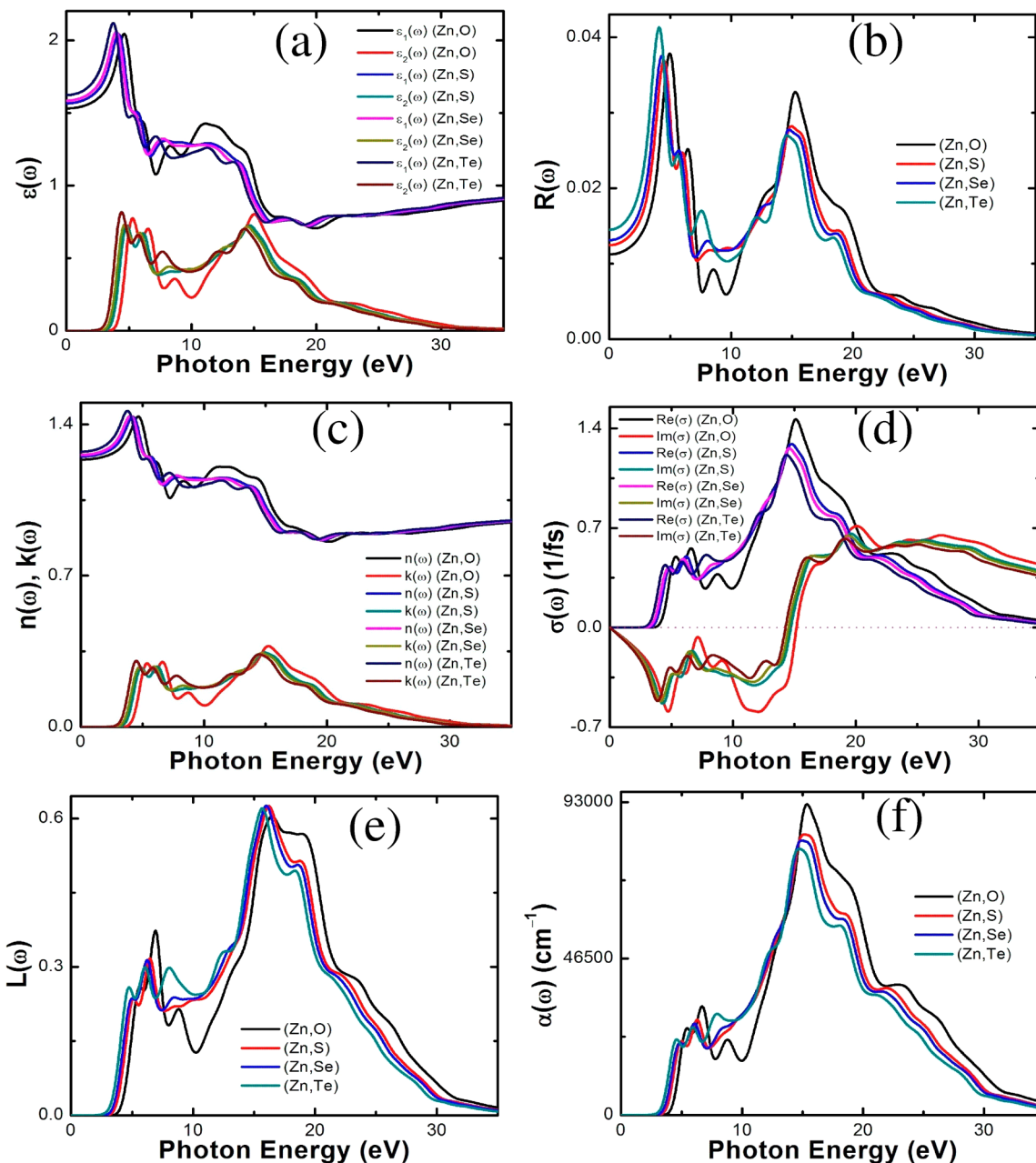


Figure 6. Calculated optical properties for (Zn, Y) subseries: (a) dielectric function $\epsilon(\omega)$, (b) reflectivity $R(\omega)$, (c) refractive index $n(\omega)$; extinction coefficient $k(\omega)$, (d) optical conductivity $\sigma(\omega)$, (e) energy loss function $L(\omega)$, and (f) absorption $\alpha(\omega)$.

occupied and unoccupied bands including appropriate momentum matrix elements to take care of the selection rules. The real part $\epsilon_1(\omega)$ can be derived from $\epsilon_2(\omega)$ using the Kramer–Kronig relationship.⁶⁹ The real part of $\epsilon(\omega)$ in the limit of zero energy (or infinite wavelength) is equal to the square of the refractive index $n(\omega)$. All the frequency-dependent linear optical properties, such as refractive index $n(\omega)$, absorption coefficient $\alpha(\omega)$, optical conductivity $\sigma(\omega)$, reflectivity $R(\omega)$, and electron energy-loss spectrum $L(\omega)$ can be deduced from $\epsilon_1(\omega)$ and $\epsilon_2(\omega)$.

The subseries (Zn, Y) is used as an example to analyze the optical properties of each material. The optical response properties of the (Zn, Y) subseries are shown in Figures 6 and 7. The results for other subseries can be found in SI Figures S54–S65. The calculated optical properties of each material are separately displayed in SI Figures S66–S86. We see that the

main characteristics are generally similar. All optical constants approach zero above 35 eV. At low photon energy below the band gaps, the imaginary part $\epsilon_2(\omega)$ of (Zn, Y) are all zero. For photon energy smaller than the band gap, there is no response under irradiation. In Figure 6, we observe the systematic tunability of the optical response, the starting points are redshifted from (Zn, O) → (Zn, Te).

The real part of the dielectric function $\epsilon_1(\omega)$ allows estimation of the values of the refractive index $n(\omega)$ at infinite wavelength or zero energy $n(0)$. In Figure 8, we plot the values of $\epsilon_1(0)$, and we see that it is increasing from 1.53 to 1.62. Meanwhile, $n(0)$ increases monotonically from 1.24 to 1.27. There are four major peaks in the $\epsilon_2(\omega)$ plot (Figure 6a) of (Zn, O), located at 5.28, 6.53, 8.66, and 15.04 eV. For (Zn, S), the main peaks of $\epsilon_2(\omega)$ are generally shifted to the left with three main peaks at 4.82, 6.12, and 14.67 eV. For the heavier

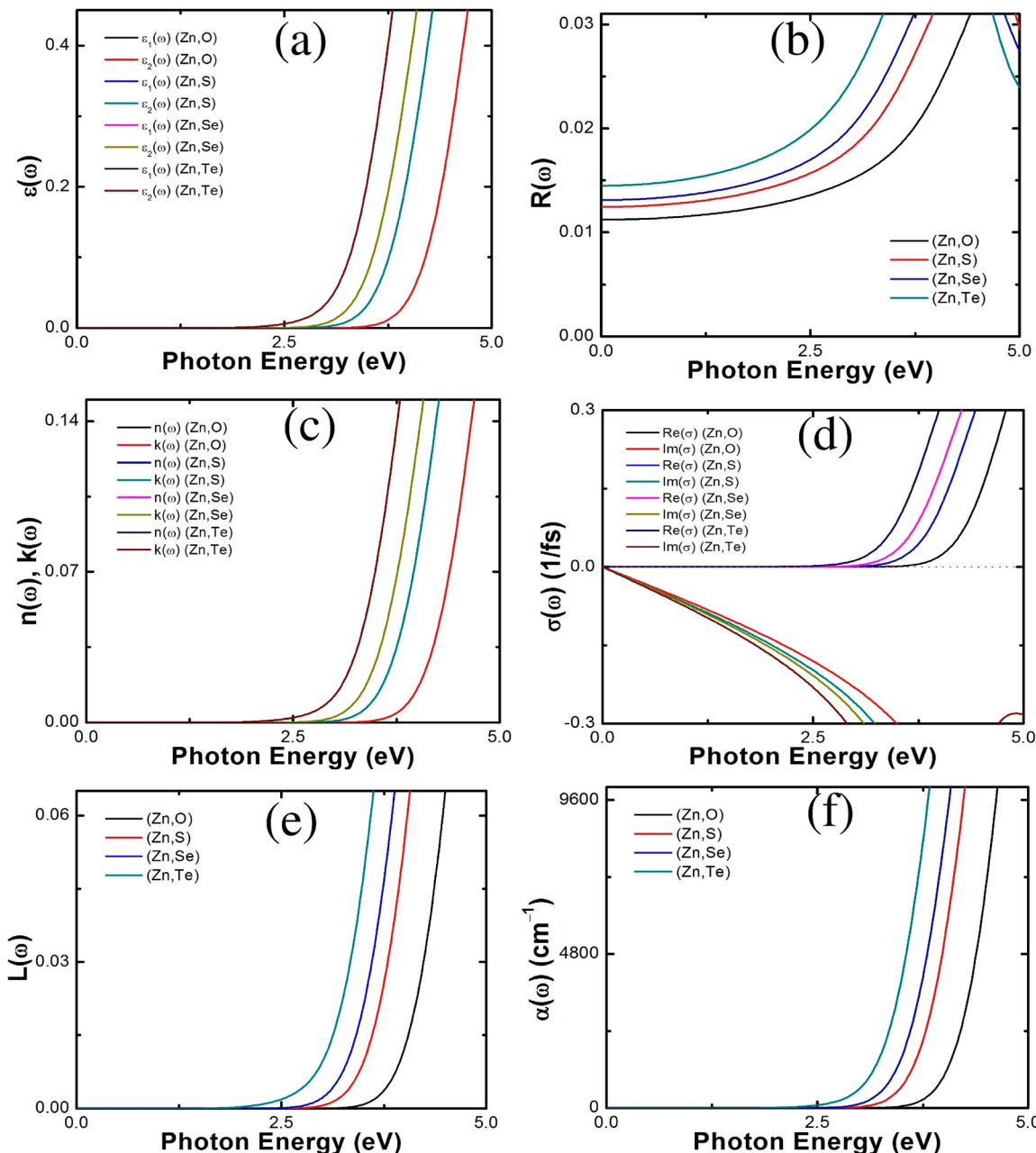


Figure 7. Optical properties for (Zn, Y) subseries between 0 and 5.0 eV: (a) dielectric function $\epsilon(\omega)$, (b) reflectivity $R(\omega)$, (c) refractive index $n(\omega)$; extinction coefficient $k(\omega)$, (d) optical conductivity $\sigma(\omega)$, (e) energy loss function $L(\omega)$, and (f) absorption $\alpha(\omega)$.

elements Se and Te, the main peaks are further shifted to even lower energies. Generally, the main characteristics of $\epsilon(\omega)$ are similar for each member within subseries, the major peaks are generally red-shifted when moving from O \rightarrow Te.

The reflectivity spectrum $R(\omega)$ (Figure 6b) of (Zn, O) shows two sharp peaks at 4.97 and 6.44 eV. These two peaks arise mainly from Zn (3d) \rightarrow O/C (2p) interband transitions from PDOS analysis. Another peak is at 8.54 eV, followed by a prominent peak seen at 15.26 eV. For the heavier element (Zn, S), the two sharp peaks are at 4.49 and 6.00 eV, which mainly arise from Zn (3d) \rightarrow S (3p)/O(2p) interband transitions. Another major peak is at 14.97 eV. In general, the main peaks of (Zn, S) are red-shifted compared to (Zn, O). For (Zn, Se) the first two peaks are at 4.31 and 5.70 eV, corresponding to the Zn (3d) \rightarrow Se (4p/3d)/O(2p) interband transitions, with additional peaks at 8.05, 14.77, and 18.58 eV. For (Zn, Te), the

major peaks of $R(\omega)$ are moved to the lowest energies. The first two sharp peaks are at 4.09 and 5.61 eV, mainly arising from Zn (3d) \rightarrow Te (5p/4d)/O(2p) interband transitions. Other major peaks are at 7.55, 12.10, 14.57, and 18.33 eV.

The values of reflectivity at zero energy $R(0)$ are shown in Figure 8c and range from 0.011 to 0.014. The $R(0)$ is slightly increasing when moving from O \rightarrow Te. This trend is similar to that of $\epsilon_1(0)$ and $n(0)$ for this subseries and the others. A general finding here is that the calculated reflectivity in the whole frequency range is much smaller than that in typical in organic solids. This may have potential applications if MOFs are to be used in optoelectronic and nanoelectronic devices (such as solar cells and LEDs) where low reflectivity is desired.

The complex refractive index includes the real part $n(\omega)$ and the imaginary part $k(\omega)$. Figure 6c shows that (Zn, O) has a nonzero value of $n(\omega)$ between 3.6 and 35 eV. The extinction

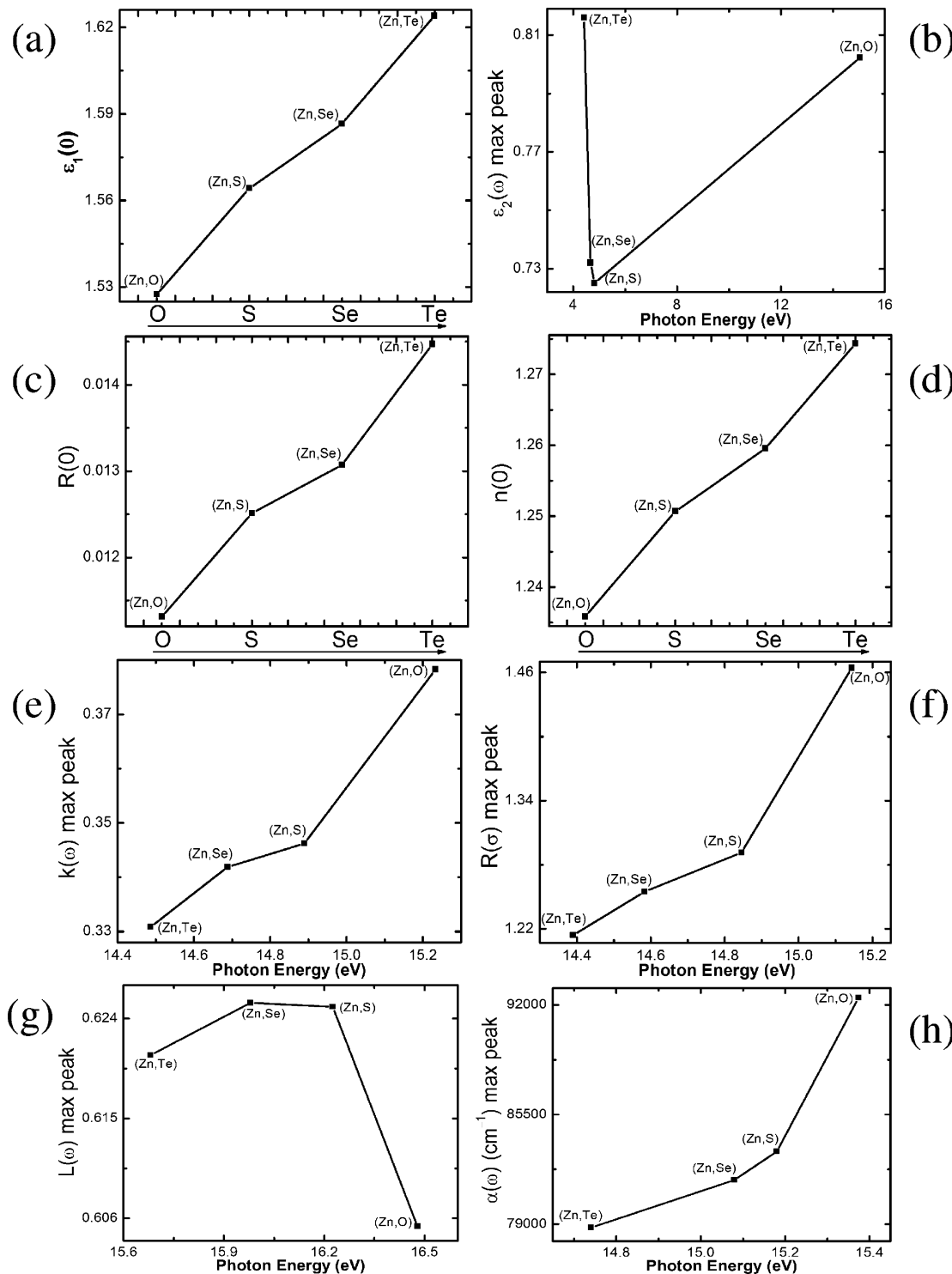


Figure 8. Special values of optical constants for (Zn, Y) subseries. We display the $\epsilon_1(0)$ in (a), the maximum peak of $\epsilon_2(\omega)$ in (b), the $R(0)$ in (c), the $n(0)$ in (d), the maximum peak of $k(\omega)$ in (e), the maximum peak of $R(\sigma)$ in (f), the maximum peak of $L(\omega)$ in (g), and the maximum peak of $\alpha(\omega)$ in (h).

coefficient $k(\omega)$ shows four main peaks at 5.38, 6.63, 8.71, and 15.26 eV. (Zn, S) has nonzero value of $n(\omega)$ between 3.1 and 35 eV. In general, the main peaks are shifted to the left compared with (Zn, O). As we expect, for (Zn, Se) and (Zn, Te), the major peaks move to even lower energies. Generally, the curves look similar for each system, with a slight red shift as we move through the series.

The optical conductivity $\sigma(\omega)$ (Zn, Y) is shown in Figure 6d. The real part of the complex conductivity $Re(\sigma)$ of (Zn, O) has four sharp peaks located at 5.36, 6.6, 8.76, and 15.14 eV. Followed by another peak located at around 22.86 eV. For the heavy elements (Zn, S), (Zn, Se), and (Zn, Te), the main peaks of optical conductivity are generally moving slightly to lower energy from O to Te.

The electron energy-loss function $L(\omega)$ (Figure 6e) is an important optical result describing the energy loss of a fast electron traversing a material. This allows comparison with experimental electron energy loss spectrometry results. The peaks of the $L(\omega)$ spectra overlap the trailing edges in the reflection spectra. Generally, below E_g , the value of $L(\omega)$ is zero, also above 35 eV, the value is negligible. For (Zn, O), there are four main peaks of $L(\omega)$ found in Figure 6e. The first two sharp peaks located at 5.64 and 6.91 eV, which correspond to the reductions in $R(\omega)$. The third peak is seen at 8.83 eV, followed by the largest peaks close together at 16.5 and roughly 19 eV. For the entire series in Figure 6e, the overall characters are generally similar, although slightly red-shifted from O → Te.

(Zn, O) has an absorption band $\alpha(\omega)$ (Figure 6f) between 3.6 and 35 eV, with four sharp peaks at about 5.48, 6.70, 8.81, and 15.38 eV. The values of $\alpha(\omega)$ are essentially zero energies above 35 eV. Whereas, (Zn, S) has an absorption band (Figure 6f) from 3.1 to 35 eV, which contains four major peaks located at 4.99, 6.29, 15.14, and 21.91 eV. The heavier elements (Zn, Se) and (Zn, Te) have absorption bands from 2.9 to 35 eV and 2.5 to 35 eV. In general, the main features of $\alpha(\omega)$ are similar to the major peaks shifted slightly to lower energies. Specific values (in SI Table S13) of each optical constant are shown in Figure 8.

IV. CONCLUSIONS

We have presented a scheme to systematically tune the band gap of prototype MOF-5 via different combinations of atoms in the nodes (X_4Y). Comprehensive DFT investigations of the electronic structure, bonding nature, ground-state properties, and optical properties of the new X_4Y -MOF-5 materials lead us to the following results:

- (1) Each material within the series is in the highly symmetric face-centered cubic $Fm\bar{3}m$ crystal structure. In general, all materials are relatively soft. The lattice parameters and bulk moduli can be tuned. Generally, the lattice parameters are increasing and bulk moduli are decreasing for each subseries moving from Y = O → S → Se → Te.
- (2) The large negative formation energies indicate the high stability of the series and will inspire and guide synthetic efforts in this direction in the future. This is consistent with the fact that paradigm MOF-5 has been experimentally available since 1999. Furthermore, the formation energy can be systematically tuned for the compounds. From Te → Se → S → O, the formation energy is monotonously increasing.
- (3) Several characterization tools (including charge density/transfer, ELF, MEC, BC, and BOP) were used to evaluate the chemical bonding of these materials. The organic linkers are primarily covalently bonded. The iconicity of the X–Y corner bonds decreases and the covalency increases when passing from Cd to Zn, and from Ba to Be; and from O to Te.
- (4) Electronic structure calculations demonstrate that the X_4Y -MOF-5 materials range from semiconductors to insulators. The band gap can be systematically tuned from 1.7 to 3.6 eV, and the corresponding minimum absorption wavelength varied from 345 to 724 nm. From O → S → Se → Te, the band gap is decreasing and the minimum absorption wavelength is increasing. The underlying mechanism of the tunability of band gap

can be ascribed to the electronic states of Y atoms in the X_4Y nodes and C atoms in the organic BDC linkers.

- (5) The optical response properties can be systematically tuned, greatly extending the absorption region of light into the visible spectrum. This suggests potential applications in nanoelectronics and optoelectronics.

ASSOCIATED CONTENT

Supporting Information

Optimized bond lengths and bond angles, the electronic band structures, the calculated TDOS and PDOS, the calculated charge density, charge transfer, and ELF plots for each subseries. Evolution of MEC, BC, BOP, and the calculated optical properties, for each series. This material is available free of charge via the Internet at <http://pubs.acs.org>.

AUTHOR INFORMATION

Corresponding Author

*E-mail: lmyang.uio@gmail.com.

Notes

The authors declare no competing financial interest.

ACKNOWLEDGMENTS

L.M.Y. gratefully acknowledges the Research Council of Norway for financial support and for the computer time at the Norwegian supercomputer facilities for the MOFs projects. L.M.Y and S.S.H are grateful for the financial support from the Korea Institute of Science and Technology (Grant no. 2E24630). G.Y.F. and J.M. thank the National Natural Science Foundation of China for financial support (Grant 21290192 and 21273102) and for the computer time at the supercomputer facilities from Nanjing University.

DEDICATION

Dedicated to Professor Alexander I. Boldyrev on the occasion of his 63rd birthday.

REFERENCES

- (1) Special Issue on MOFs. *Chem. Soc. Rev.* **2009**, *38* (5), 1201–1508.
- (2) Special Issue on MOFs. *Chem. Rev.* **2012**, *112* (2), 673–1268.
- (3) Mahata, P.; Madras, G.; Natarajan, S. *J. Phys. Chem. B* **2006**, *110*, 13759.
- (4) Alvaro, M.; Carbonell, E.; Ferrer, B.; Llabres i Xamena, F. X.; Garcia, H. *Chem.—Eur. J.* **2007**, *13*, 5106.
- (5) Gascon, J.; Hernández-Alonso, M. D.; Almeida, A. R.; van Klink, G. P. M.; Kapteijn, F.; Mul, G. *ChemSusChem* **2008**, *1*, 981.
- (6) Wang, J.-L.; Wang, C.; Lin, W. *ACS Catal.* **2012**, *2*, 2630.
- (7) Bordiga, S.; Lamberti, C.; Ricchiardi, G.; Regli, L.; Bonino, F.; Damin, A.; Lillerud, K. P.; Bjorgen, M.; Zecchina, A. *Chem. Commun.* **2004**, 2300.
- (8) Li, H.; Eddaoudi, M.; O'Keeffe, M.; Yaghi, O. M. *Nature* **1999**, *402*, 276.
- (9) Feng, P. L.; Perry, J. J., IV; Nikodemski, S.; Jacobs, B. W.; Meek, S. T.; Allendorf, M. D. *J. Am. Chem. Soc.* **2010**, *132*, 15487.
- (10) Ji, M.; Lan, X.; Han, Z.; Hao, C.; Qiu, J. *Inorg. Chem.* **2012**, *51*, 12389.
- (11) Khajavi, H.; Gascon, J.; Schins, J. M.; Siebbeles, L. D. A.; Kapteijn, F. *J. Phys. Chem. C* **2011**, *115*, 12487.
- (12) Heine, J.; Muller-Buschbaum, K. *Chem. Soc. Rev.* **2013**, *42*, 9232.
- (13) Kresse, G.; Furthmüller, J. *Comput. Mater. Sci.* **1996**, *6*, 15.
- (14) Kresse, G.; Joubert, D. *Phys. Rev. B* **1999**, *59*, 1758.
- (15) Perdew, J. P. In *Electronic Structure of Solids*; Ziesche, P., Eschrig, H., Eds.; Akademie Verlag: Berlin, 1991; p 11.

- (16) Perdew, J. P.; Burke, K.; Wang, Y. *Phys. Rev. B* **1996**, *54*, 16533.
- (17) Perdew, J. P.; Burke, K.; Ernzerhof, M. *Phys. Rev. Lett.* **1996**, *77*, 3865.
- (18) Blochl, P. E. *Phys. Rev. B* **1994**, *50*, 17953.
- (19) Yang, L.-M.; Vajeeston, P.; Ravindran, P.; Fjellvag, H.; Tilset, M. *Phys. Chem. Chem. Phys.* **2011**, *13*, 10191.
- (20) Blomqvist, A.; Araújo, C. M.; Srepusharawoot, P.; Ahuja, R. *Proc. Natl. Acad. Sci. U.S.A.* **2007**, *104*, 20173.
- (21) Becke, A. D.; Edgecombe, K. E. *J. Chem. Phys.* **1990**, *92*, 5397.
- (22) Savin, A.; Becke, A. D.; Flad, J.; Nesper, R.; Preuss, H.; Vonschnering, H. G. *Angew. Chem., Int. Ed. Engl.* **1991**, *30*, 409.
- (23) Savin, A.; Jepsen, O.; Flad, J.; Andersen, O. K.; Preuss, H.; Vonschnering, H. G. *Angew. Chem., Int. Ed. Engl.* **1992**, *31*, 187.
- (24) Silvi, B.; Savin, A. *Nature* **1994**, *371*, 683.
- (25) Yang, L.-M.; Vajeeston, P.; Ravindran, P.; Fjellvag, H.; Tilset, M. *Inorg. Chem.* **2010**, *49*, 10283.
- (26) Yang, L.-M.; Ravindran, P.; Vajeeston, P.; Tilset, M. *RSC Adv.* **2012**, *2*, 1618.
- (27) Yang, L.-M.; Ravindran, P.; Vajeeston, P.; Tilset, M. *Phys. Chem. Chem. Phys.* **2012**, *14*, 4713.
- (28) Yang, L.-M.; Ravindran, P.; Vajeeston, P.; Tilset, M. *J. Mater. Chem.* **2012**, *22*, 16324.
- (29) Yang, L.-M.; Ravindran, P.; Vajeeston, P.; Svelle, S.; Tilset, M. *Microporous Mesoporous Mater.* **2013**, *175*, 50.
- (30) Yang, L.-M.; Ravindran, P.; Tilset, M. *Inorg. Chem.* **2013**, *52*, 4217.
- (31) Yang, L.-M. *Microporous Mesoporous Mater.* **2014**, *183*, 218.
- (32) Yang, L.-M.; Pushpa, R. *J. Mater. Chem. C* **2014**, *2*, 2404.
- (33) It should be pointed out that there is a bug regarding CASTEP calculations on BOP values of M-O (M is the alkaline-earth metals) with Ultrasoft pseudopotential. The customer service of Materials Studio made many tests on this problem, finally, they suggested to use on the fly pseudopotential to fix this problem. There is no bug on the calculations of optical properties and band structures with Ultrasoft pseudopotential, which keeps a balance between speed and accuracy of the calculations. Thus, we choose Ultrasoft pseudopotential for the calculations of optical properties and band structures, and on the fly pseudopotential for the calculations of population analysis (include MEC, BOP, and EC) for the current systems.
- (34) Segall, M. D.; Lindan, P. J. D.; Probert, M. J.; Pickard, C. J.; Hasnip, P. J.; Clark, S. J.; Payne, M. C. *J. Phys.: Condens. Matter* **2002**, *14*, 2717.
- (35) Materials Studio, ver. 5.0; Accelrys: San Diego, CA, 2009.
- (36) Murnaghan, F. D. *Proc. Natl. Acad. Sci. U.S.A.* **1944**, *30*, 244.
- (37) Birch, F. *Phys. Rev.* **1947**, *71*, 809.
- (38) Vinet, P.; Rose, J. H.; Ferrante, J.; Smith, J. R. *J. Phys.: Condens. Matter* **1989**, *1*, 1941.
- (39) Sumida, K.; Hill, M. R.; Horike, S.; Dailly, A.; Long, J. R. *J. Am. Chem. Soc.* **2009**, *131*, 15120.
- (40) Porter, W. W., III; Wong-Foy, A.; Dailly, A.; Matzger, A. J. *J. Mater. Chem.* **2009**, *19*, 6489.
- (41) Dietzel, P. D. C.; Blom, R.; Fjellvåg, H. *Eur. J. Inorg. Chem.* **2008**, *2008*, 3624.
- (42) Dincă, M.; Long, J. R. *J. Am. Chem. Soc.* **2005**, *127*, 9376.
- (43) Britt, D.; Furukawa, H.; Wang, B.; Glover, T. G.; Yaghi, O. M. *Proc. Natl. Acad. Sci. U.S.A.* **2009**, *106*, 20637.
- (44) Mallick, A.; Saha, S.; Pachfule, P.; Roy, S.; Banerjee, R. *J. Mater. Chem.* **2010**, *20*, 9073.
- (45) Banerjee, D.; Finkelstein, J.; Smirnov, A.; Forster, P. M.; Borkowski, L. A.; Teat, S. J.; Parise, J. B. *Cryst. Growth Des.* **2011**, *11*, 2572.
- (46) Plonka, A. M.; Banerjee, D.; Parise, J. B. *Cryst. Growth Des.* **2012**, *12*, 2460.
- (47) Vakiti, R. K.; Garabato, B. D.; Schieber, N. P.; Rucks, M. J.; Cao, Y.; Webb, C.; Maddox, J. B.; Celestian, A.; Pan, W.-P.; Yan, B. *Cryst. Growth Des.* **2012**, *12*, 3937.
- (48) Chen, X.; Plonka, A. M.; Banerjee, D.; Parise, J. B. *Cryst. Growth Des.* **2012**, *13*, 326.
- (49) Chen, Y.; Chen, W.; Ju, Z.; Gao, Q.; Lei, T.; Liu, W.; Li, Y.; Gao, D.; Li, W. *Dalton Trans.* **2013**, *42*, 10495.
- (50) Appelhans, L. N.; Kosa, M.; Radha, A. V.; Simoncic, P.; Navrotsky, A.; Parrinello, M.; Cheetham, A. K. *J. Am. Chem. Soc.* **2009**, *131*, 15375.
- (51) Rybak, J.-C.; Hailmann, M.; Matthes, P. R.; Zurawski, A.; Nitsch, J.; Steffen, A.; Heck, J. G.; Feldmann, C.; Götzendörfer, S.; Meinhardt, J.; Sextl, G.; Kohlmann, H.; Sedlmaier, S. J.; Schnick, W.; Müller-Buschbaum, K. *J. Am. Chem. Soc.* **2013**, *135*, 6896.
- (52) Zhang, Z. T.; Wang, Q. Y.; Li, W. W.; Meng, Q. H.; Zhang, X. L. *CrystEngComm* **2012**, *14*, 5042.
- (53) Wu, G.; Yin, F. J.; Li, H. H.; Guo, L. *J. Chem. Crystallogr.* **2012**, *42*, 680.
- (54) Saha, D.; Maity, T.; Sen, R.; Koner, S. *Polyhedron* **2012**, *43*, 63.
- (55) Maity, T.; Saha, D.; Das, S.; Koner, S. *Eur. J. Inorg. Chem.* **2012**, *4914*.
- (56) Foo, M. L.; Horike, S.; Duan, J. G.; Chen, W. Q.; Kitagawa, S. *Cryst. Growth Des.* **2013**, *13*, 2965.
- (57) Kuc, A.; Enyashin, A.; Seifert, G. *J. Phys. Chem. B* **2007**, *111*, 8179.
- (58) Yeung, H. H. M.; Kosa, M.; Parrinello, M.; Forster, P. M.; Cheetham, A. K. *Cryst. Growth Des.* **2010**, *11*, 221.
- (59) Odbadrakh, K.; Lewis, J. P.; Nicholson, D. M. *J. Phys. Chem. C* **2010**, *114*, 7535.
- (60) Levine, Z. H.; Allan, D. C. *Phys. Rev. Lett.* **1989**, *63*, 1719.
- (61) Heyd, J.; Scuseria, G. E.; Ernzerhof, M. *J. Chem. Phys.* **2003**, *118*, 8207.
- (62) Heyd, J.; Peralta, J. E.; Scuseria, G. E.; Martin, R. L. *J. Chem. Phys.* **2005**, *123*, 174101.
- (63) Heyd, J.; Scuseria, G. E.; Ernzerhof, M. *J. Chem. Phys.* **2006**, *124*, 219906.
- (64) Shishkin, M.; Kresse, G. *Phys. Rev. B* **2007**, *75*, 235102.
- (65) Bader, R. F. W. In *Atoms in Molecules: A Quantum Theory*; Clarendon Press: Oxford, 1990.
- (66) Henkelman, G.; Arnaldsson, A.; Jonsson, H. *Comput. Mater. Sci.* **2006**, *36*, 354.
- (67) Fonseca Guerra, C.; Handgraaf, J.-W.; Baerends, E. J.; Bickelhaupt, F. M. *J. Comput. Chem.* **2004**, *25*, 189.
- (68) Mulliken, R. S. *J. Chem. Phys.* **1955**, *23*, 1833.
- (69) Yu, P. Y.; Cardona, M. *Fundamentals of Semiconductors*; Springer-Verlag: Berlin, 1996.